

Visualization of conformational changes and membrane remodeling leading to genome delivery by viral class-II fusion machinery

Vidya Mangala Prasad

Indian Institute of Science

Jelle Blijleven

University of Groningen

Jolanda Smit

University of Groningen

Kelly Lee (✉ kklee@uw.edu)

University of Washington <https://orcid.org/0000-0001-5577-9873>

Article

Keywords:

Posted Date: March 10th, 2022

DOI: <https://doi.org/10.21203/rs.3.rs-1414199/v1>

License:  This work is licensed under a Creative Commons Attribution 4.0 International License.

[Read Full License](#)

Version of Record: A version of this preprint was published at Nature Communications on August 15th, 2022. See the published version at <https://doi.org/10.1038/s41467-022-32431-9>.

1
2
3
4
5
6
7
8
9
10
11
12
13
14
15
16
17
18
19
20
21
22

Visualization of conformational changes and membrane remodeling leading to genome delivery by viral class-II fusion machinery

Vidya Mangala Prasad¹¥, Jelle S. Blijleven², Jolanda M. Smit³, Kelly K. Lee^{1,4,5*}

Affiliations:

1. Department of Medicinal Chemistry, University of Washington, Seattle, WA 98195, USA.
2. Zernike Institute for Advanced Materials, University of Groningen, Groningen, The Netherlands.
3. Department of Medical Microbiology and Infection Prevention, University of Groningen, University Medical Center Groningen, Groningen, The Netherlands.
4. Biological Physics, Structure and Design Graduate Program, University of Washington, Seattle, WA 98195, USA.
5. Department of Microbiology, University of Washington, Seattle, WA 98195, USA.

¥Current Address: Molecular Biophysics Unit, Indian Institute of Science, Bengaluru 560012, Karnataka, India.

*Correspondence to: kklee@uw.edu

23 **Abstract:**

24 Chikungunya virus (CHIKV) is a human pathogen that delivers its genome to the host cell
25 cytoplasm through endocytic low pH-activated membrane fusion mediated by class-II fusion
26 proteins. Though structures of prefusion, icosahedral CHIKV are available, structural
27 characterization of virion interaction with membranes has been limited. Here, we have used cryo-
28 electron tomography to visualize CHIKV's complete membrane fusion pathway, identifying key
29 intermediary glycoprotein conformations coupled to membrane remodeling events. Using sub-
30 tomogram averaging, we elucidate features of the low pH-exposed virion, nucleocapsid and full-
31 length E1-glycoprotein's post-fusion structure. Contrary to class-I fusion systems, CHIKV
32 achieves membrane apposition by protrusion of extended E1-glycoprotein homotrimers into the
33 target membrane. The fusion process also features a large hemifusion diaphragm that transitions
34 to a wide pore for intact nucleocapsid delivery. Our analyses provide comprehensive ultrastructural
35 insights into the class-II virus fusion system function and direct mechanistic characterization of
36 the fundamental process of protein-mediated membrane fusion.

37

38

39 **Introduction:**

40 Chikungunya virus (CHIKV) is a mosquito-borne human pathogen that has caused major
41 outbreaks in Europe, Asia and the Americas^{1,2}. It is a member of the alphavirus genus in the
42 *Togaviridae* family³. Along with other members including Ross River virus, Semliki Forest virus,
43 Sindbis virus and Venezuelan equine encephalitis virus, alphaviruses are responsible for severe
44 emerging diseases in humans and animals^{1,4,5}. CHIKV infections are characterized by high fever,
45 fatigue, joint and muscle pains, with serious long-term effects including debilitating
46 polyarthralgia^{6,7}. Despite its medical importance, no vaccines or antivirals against any alphavirus
47 is currently available^{8,9}.

48 CHIKV, like all alphaviruses, is a membrane-enveloped, single-stranded, positive-sense
49 RNA virus with an ~11.8kb genome^{3,10}. The mature CHIKV virion is composed of an icosahedral
50 inner nucleocapsid containing 240 capsid monomers that enclose the viral genome¹¹. The
51 nucleocapsid is surrounded by a membrane bilayer. The external surface of the mature virus
52 contains 240 copies of E1 and E2 membrane-anchored glycoprotein heterodimers, arranged as 80
53 trimeric spikes following icosahedral symmetry^{3,10,11} (Figure 1a-c). E2 is primarily responsible for
54 cellular receptor attachment^{12,13} but also interacts non-covalently with the nucleocapsid to
55 stabilize the virion structure¹⁴. The E1 glycoprotein contains the hydrophobic fusion loop (FL)
56 and mediates membrane fusion^{15,16}. In the mature virion, E2 is positioned above E1, shielding the
57 functionally critical FL from premature exposure^{11,17} (Figure 1b,c).

58 CHIKV enters host cells primarily via clathrin-mediated endocytosis¹⁸ following
59 attachment to a cellular receptor such as MxRA8¹⁹ or other attachment factors such as heparan
60 sulfate or C-type lectins²⁰. Upon cellular entry, the virus is engulfed into endosomes where the low
61 pH environment resulting from endosomal maturation triggers conformational changes on the

62 virus surface including the dissociation of the E1-E2 heterodimer²¹ and the formation of extended
63 E1 homotrimers (HT) with its FLs inserted into the target membrane^{22,23} (Figure 1d,e). The E1-
64 HTs are then thought to drive membrane fusion by refolding/hairpin formation to bring the
65 opposing membranes together²². Lipid mixing between the viral and endosomal membrane results
66 in fusion pore formation that allows delivery of the viral nucleocapsid into the cytoplasm where it
67 subsequently disassembles to release the viral RNA and establish infection^{24,25}.

68 The current model for how alphavirus membrane fusion takes place is primarily based on
69 x-ray crystallographic structures of the pre-fusion²⁶ and post-fusion conformations of recombinant
70 E1 glycoprotein ectodomains²² along with related molecular studies on isolated glycoproteins^{23,27}.
71 We lack direct structural data describing the sequence of protein conformational changes and
72 nature of membrane remodeling that is necessary to derive a mechanistic understanding of the
73 fusion process for alphaviruses and, more broadly, the type of fusion system (class-II) they
74 represent²⁸.

75 Here, we have used cryo-electron tomography (cryo-ET) in combination with sub-
76 tomogram averaging to trap and observe the membrane fusion process in CHIKV under near-
77 native conditions. Through stepwise analysis of CHIKV interactions with a target membrane at
78 varying pH values and reaction timepoints, we can clearly demarcate intermediate stages in
79 CHIKV membrane fusion. These data provide comprehensive insights into changes in virion
80 structure, glycoprotein conformations, and changes in membrane organization along the fusion
81 pathway. Our results also demonstrate that membrane fusion mediated by class-II fusion proteins
82 in CHIKV proceeds by a markedly different pathway than class-I fusion systems such as influenza
83 virus²⁹⁻³². Furthermore, our results highlight the power of cryo-ET for capturing 3-dimensional
84 snapshots of reaction intermediates in a dynamic biological process from start to finish.

85 **Results:**

86 For our experiments, CHIKV (strain S27) particles were rendered replication incompetent
87 by UV-light inactivation. The UV-treated virus drives membrane fusion in a similar fashion to
88 untreated virus³³. Single particle cryo-EM reconstruction of the UV-treated CHIKV was calculated
89 to a resolution of 6.75 Å, which confirmed that the virion structure at neutral pH is identical to
90 reported CHIKV structures^{11,19} (Figure 1a, Supplementary Figure 1).

91 CHIKV particles were mixed with liposomes at varying pH conditions and incubated for a
92 range of time points prior to plunge freezing in liquid ethane. Liposomes were prepared based on
93 previous reports for optimal fusion in CHIKV³³. At pH 6.5 and below, rapid aggregation of CHIKV
94 particles was observed, hence, optimization of the ratio of liposomes to CHIKV was performed to
95 reduce aggregation. The pH threshold for CHIKV S27 fusion is 6.2 with optimal fusion occurring
96 in the pH range of 4.5-5.6³³. Within this range, most particles carry out fusion within 10 seconds
97 of exposure to low pH at 37 °C³³, exhibiting similar kinetics to other alphaviruses^{34,35}. To better
98 sample and capture intermediate fusion stages within the constraints of cryo-EM grid preparation
99 conditions, membrane fusion experiments were performed at room temperature, which slows the
100 fusion reaction.

101 At pH values above 6.0, CHIKV particles associated with liposomes via discrete densities
102 bridging the virus-liposome interface (Supplementary Figure 2). However, interactions beyond the
103 initial virus-liposome association were rarely observed even at longer incubation periods of ~30
104 minutes. Indeed, even in fluorescence studies, the extent of fusion events observed at pH 6.0 and
105 above was negligible³³. We observed a clear progression to completion of fusion only at pH values
106 below 6.0. At pH ≤ 5.0 , even at room temperature, most virions in the population completed the
107 membrane fusion process within 15 seconds. Thus, for better sampling of fusion events, pH values

108 in the intermediate range including 5.9, 5.6 and 5.1 were examined. Across these pH values, the
109 observed intermediates are similar, except that at lower pH, a more rapid progression through steps
110 leading to complete fusion was observed. From analysis of more than six hundred CHIKV-
111 liposome complexes in our tomograms, CHIKV-mediated membrane fusion stages could be
112 categorized into nine distinct steps, which are discussed in detail below.

113

114 Stage I - Membrane recruitment:

115 Initial membrane recruitment can be observed between 30 seconds-1 minute at pH 6.1 and
116 5.9, and within 30 seconds at pH 5.6. Minute, localized attachments are observed, sparsely
117 bridging the CHIKV glycoprotein exterior to the liposomes, with the glycoprotein shell appearing
118 relatively intact (Figure 2a-c, Supplementary Video 1). From analysis of more than one hundred
119 such interactions, the lengths of the delicate attachments extending from the viral glycoprotein
120 surface to the liposome surface were observed to be ~32-45 Å. At neutral pH on the virus surface,
121 the E2 B domain protects the E1-FL from solvent exposure¹¹ (Figure 1b), but under low pH
122 conditions, the B domain has been reported to exhibit increased flexibility resulting in E1-FL
123 exposure and potential for membrane binding^{17,36}. The fine attachments seen in the tomograms
124 (Figure 2a-c) thus likely reflect a state in which the tip of individual E1s containing the FL have
125 inserted into membrane, but without global disruption of the trimeric E1-E2 arrangement on the
126 virus surface (Figure 2d).

127 While the CHIKV surface appeared globally intact, sub-tomogram averaging of low pH
128 (<6.0) exposed CHIKV particles that were isolated or weakly attached to target membranes,
129 showed that the virions have deviated from their global icosahedrally symmetrical organization
130 (Supplementary Figure 3D). Due to the low number of particles available, it was not possible to

131 determine whether the virions retained local symmetry features. Comparison of 2D radial density
132 plots of neutral pH CHIKV with the sub-tomogram averaged low pH CHIKV structure showed
133 that the outer glycoprotein shell in low pH CHIKV had expanded by ~ 20 Å relative to neutral pH
134 CHIKV (Supplementary Figure 3).

135

136 Stage II - Membrane attachment:

137 The next stage of glycoprotein engagement with the target membrane is accompanied by a
138 transition of E1 from its orientation parallel to the virus surface to a more perpendicular orientation
139 with respect to the surface. This stage occurred by 1 minute at pH 5.9, by 30 seconds at pH 5.6
140 and almost instantaneously at pH 5.1.

141 In $\sim 2\%$ of examples of CHIKV at early time points, singular, hyper-extended glycoprotein
142 density was seen interacting with the target liposome. The connecting density in these cases were
143 ~ 170 Å - 250 Å as measured from the viral membrane surface to the liposomal membrane (Figure
144 2e). In contrast, crystal structures of the E1 ectodomain in its pre-fusion and post-fusion
145 conformations have a length of only ~ 125 Å²⁶ and ~ 100 Å²² respectively (Figure 1b,d). Thus, these
146 extended connections are only feasible with major changes in the E1 structure involving
147 hyperextension and repositioning of component domains. This also suggests that the energy
148 needed to detach E1 from the target membrane is larger than that required to partially unravel the
149 E1 subunit.

150 More commonly at this stage, extensions of clustered glycoprotein density and formation
151 of multiple robust attachments were observed between the glycoproteins and the liposomes at the
152 interaction interface (Figure 3a-c, Supplementary Video 2). For virion facets that were not
153 interacting with membranes, heterogeneity in glycoprotein organization was evident on the particle

154 exterior. From analysis of 221 interaction sites, consisting of multiple glycoprotein attachments to
155 liposomes, the length of these connecting densities ranged between 90 Å to 165 Å on central
156 tomogram slices (perpendicular to electron beam direction), as measured from the viral membrane
157 surface to the target membrane. Corroborating our observations, long, bridge-like densities,
158 attributed to the E1 protein, have been imaged previously in an early-stage fusion intermediate of
159 Sindbis virus in contact with liposomes³⁷. Furthermore, in our tomograms, residual protein density
160 was seen close to the viral membrane at the virus-liposome interface (Figure 3a-c) suggesting that
161 the E2 proteins may still be present at the particle-liposome interface, similar to that seen with
162 Sindbis virus³⁷. The observed multiple attachments between E1 and liposome membrane appear to
163 set the stage for further steps that involve concerted action of multiple E1 proteins.

164

165 Stage III – E1 homotrimer (HT) formation:

166 Once multiple attachments between E1 and target membrane have formed, the E1
167 glycoproteins at the virus-target membrane interface transition to form thick, cone-like densities
168 that are perpendicular to the viral and target membrane planes (Figure 3e-g, I, Supplementary
169 Video 3). These features (Figure 3e-g) are similar in shape to the known crystal structures of post-
170 fusion E1 trimers (Figure 1d,e) suggesting that the E1 proteins have oligomerized at this stage to
171 a form of E1 homotrimers (HT). Four to five E1-HTs can be identified clustered at a given virus-
172 liposome interface (Figure 3e-g). The E2 proteins appear to have been displaced from the virus-
173 liposome interface to allow E1 trimerization. E1-HTs were observed by 2 minutes at pH 5.9 as
174 well as pH 5.6 and by 30 seconds-1 minute at pH 5.1.

175 At the resolution of our cryo-ET data, it is not possible to directly discern whether swapping
176 of domains I and III of E1, as seen in the crystal structures of post-fusion E1 ectodomain trimers

177 ²², has occurred. The lengths of E1-HTs in our tomograms are ~130-150 Å whereas the length of
178 the post-fusion E1-trimers from crystal structures measures ~100 Å (Figure 1d). The E1-domain
179 III is ~30Å in dimension. The cryo-ET data, thus, indicate that the domain III of E1 has likely not
180 folded back to produce the post-fusion conformation at this stage. Our inference regarding this
181 extended E1-HT state is supported by the identification of a pre-fusion intermediate form of E1-
182 HT in previous molecular studies with Semliki Forest virus and Sindbis viruses^{27,35}.

183

184 Stage IV - E1-HT membrane insertion:

185 Once extended E1-HT formation occurs, the trimer appears to drive through the target
186 membrane, causing depressions and possibly small punctures to the target membrane integrity
187 (Figure 4a-e, Supplementary Video 3,4). This stage of E1-HT membrane insertion can be observed
188 by 2-5 minutes at pH 5.6 and by 30 seconds-1 minute at pH 5.1. Supporting our observations,
189 insertion of purified low pH-induced E1 homotrimers (full-length and ectodomain) into liposomal
190 membranes has been previously reported ^{22,38}. Exact measurements of glycoprotein length in this
191 stage were challenging owing to interference from surrounding membrane density. However, in
192 cases where measurements could be made, such as in examples shown in Figure 4b-d, the E1-HT
193 length varied from 110-150Å suggesting that complete folding-back of E1-domain III had still not
194 occurred. In our cryo-ET data, we also observe examples of neighboring glycoprotein densities
195 attaching to the target membrane (Figure 4b-d). With increasing numbers of glycoprotein
196 attachments to the target membrane, the membrane is pulled towards the virion and can be
197 observed to follow the contours of the virion exterior (Figure 4b-d). Projection of E1-HT into the
198 target membrane at these closely packed interfaces appears to be responsible for bringing the target
199 membrane close to the viral membrane.

200 Stage V and VI - Opposing membrane superposition:

201 In similar timepoints as E1-HT membrane insertion, opposing membrane superposition
202 was also observed. As the membrane-inserted conformation of E1-HTs are not a favorable
203 condition for the predominantly surface exposed E1 proteins, we deduce that the E1-HTs likely
204 are driven away from the virus-liposome interface, resulting in their exclusion from the contact
205 zone, which instead contains the two membranes in close proximity to each other with only an ~1
206 nm gap between the proximal leaflets (Figure 4f-i, Supplementary Video 5).

207 At these intermediate stages, starting from the stage of extended E1-HT formation, we
208 observe glycoproteins being displaced laterally on the virion surface (Figure 4f,g). This indicates
209 that the cytoplasmic tails of the E2 glycoproteins have been uncoupled from the internal
210 nucleocapsid, affording them mobility that is restricted in prefusion CHIKV and early fusion
211 stages. In a few cases, a larger gap between the nucleocapsid and viral membrane is seen (Figure
212 4f,g) with the nucleocapsid no longer juxtaposed against the inner side of the viral membrane.

213 At this stage, we concurrently also observed cases where the viral and target membrane
214 bilayers were tightly docked together, such that the individual proximal leaflets were
215 indistinguishable at the resolution of our tomograms, resulting in a distinct 3-layer membrane
216 interface (Figure 4j-l, Supplementary Video 6). Such a configuration requires dehydration of the
217 proximal leaflets to permit close approach and meshing of the polar headgroups³⁹. Most likely the
218 energy released from the surrounding glycoprotein activity is transduced into formation of this
219 lipidic organization⁴⁰. Similar tightly-docked membrane-membrane contacts have been reported
220 previously as an intermediate during membrane fusion by influenza virus³⁰ and intracellular
221 SNARE proteins³⁹.

222

223 Stage VII - Hemifusion:

224 Following the formation of tightly juxtaposed membrane interfaces, we next observe clear
225 examples of merged outer leaflets of the viral and liposomal membranes, corresponding to
226 hemifused membranes (Figure 5a,b, Supplementary Video 7). This stage is observed at 5 minutes
227 at pH 5.6 and by 3 minutes at pH 5.1. It is possible that target-membrane insertion of E1-HTs
228 followed by movement of E1-HTs away from the interface causes enough perturbation or strains
229 in the membrane to encourage lipid mixing and merging of the proximal leaflets. At the junction
230 between the viral and target membranes, we observed clear examples of E1-homotrimers that
231 measure ~ 100 Å (Fig. 5a), consistent with the size and shape of post-fusion E1 trimers²². This
232 indicates that by the hemifusion stage, the extended E1-HTs have transitioned completely, with
233 domain III folded back, to form post-fusion E1 trimers, driving tight membrane apposition and
234 hemifusion.

235 Remarkably, the hemifusion diaphragm in CHIKV membrane fusion is quite large. In cases
236 where this interface was resolved clearly in all directions, the diaphragm appeared almost circular
237 with an average diameter of 350 Å, which is nearly half the CHIKV diameter (Figure 5c). In
238 general, hemifusion diaphragms ranged from half to full diameter of CHIKV, making them
239 comparable in size to the nucleocapsid that needs to be delivered once the fusion pore forms
240 (Figure 5a).

241

242 Stage VIII – Fusion pore formation:

243 Hemifusion in CHIKV progresses with disintegration of the hemifusion diaphragm,
244 leading to formation of a fusion pore (Figure 5d,e; Supplementary Video 8). This stage is observed

245 by 5 minutes at pH 5.6 and 3 minutes at pH 5.1. In agreement with the large hemifusion
246 diaphragms, fusion pores also exhibit widths >75% of the virion diameter (Figure 5d).

247

248 Stage IX – Release of intact nucleocapsid:

249 The last step of membrane fusion is the release of the CHIKV nucleocapsid (NC) into the
250 liposome lumen. We observed more than 150 instances of NC released into the liposomal lumen
251 and all of them appeared intact (Figure 5f,g; Supplementary Video 9). Nevertheless, the released
252 NCs had lost icosahedral symmetry, as confirmed by our sub-tomogram averaging attempts of
253 intact NCs. The presence of intact cores after membrane fusion confirm that further interaction
254 with cellular host factors, such as the large ribosomal subunit ²⁴, is required for nucleocapsid
255 disassembly and release of the viral genome. The loss of icosahedral symmetry in the intact NCs
256 further substantiates conformational changes in its structure as has been proposed previously to be
257 necessary for exposing interaction sites that facilitate NC disassembly ²⁵.

258 In the timepoints where membrane fusion has been completed and the intact NCs have
259 been released into the liposome lumen, distinct protein densities decorate the exterior of fused
260 liposomes (Figure 5f, Supplementary Video 9). These protein subunits originate at the virus-
261 liposome fusion interface and are distributed across the entire fused liposome (Figure 5f). From
262 top-down views of fused liposome surfaces in our tomograms, the protein subunits appear trimeric
263 (Figure 5g). Sub-volumes of these protein subunits were extracted from the cryo-electron
264 tomograms and subjected to sub-tomogram averaging. The resolution of the averaged structure is
265 27.2 Å at 0.5 FSC (Fourier Shell Correlation) cutoff (Supplementary Figure 4). The crystal
266 structure of the post-fusion E1 homotrimer from Semliki Forest Virus (SFV) (PDB ID:1RER) fits
267 in a unique orientation into the density map (Figure 5h), confirming that these protein subunits are

268 indeed the post-fusion E1-trimers. Fitting the E1 ectodomain crystal structure into the density map
269 shows that insertion of the E1 trimer into the outer membrane leaflet is only mediated by its FL
270 without embedding additional regions of the ectodomain (Figure 5h). Moreover, no extra density
271 is left to accommodate the E2 protein. These observations indicate that during and after membrane
272 fusion, the E2 proteins do not form any oligomeric conformations and likely remain as individual
273 protein subunits diffused across the membrane surface²¹.

274

275 Other effects of low pH on CHIKV:

276 At longer timepoints of pH 5.6 and 5.1, CHIKV can be often observed to undergo
277 membrane fusion steps as a cluster of aggregated virions (Supplementary Figure 5a). Virions fused
278 with each other suggesting that membrane attachment of E1 is non-specific (Supplementary Figure
279 5b). Furthermore, instances where one virion facilitated attachment and membrane fusion of an
280 adjacent virion were also observed (Supplementary Figure 5a). Instances where CHIKV particles
281 released NCs into the solution without any interaction with liposomes were also seen
282 (Supplementary Figure 5b), suggesting that the CHIKV virion becomes increasingly unstable with
283 decreasing pH.

284

285 **Discussion:**

286 Protein-mediated membrane fusion is a critical step in enveloped virus infection and a
287 fundamental process that underpins many cellular functions. For viruses that employ class-II
288 fusion proteins, such as flavi- and alphaviruses, virion architectures and structures of the pre- and
289 post-fusion glycoprotein ectodomains are well established^{28,41}. However, as with most protein-
290 mediated fusion systems, it has been challenging to obtain detailed structural information that

291 describes the sequence of events that occur during membrane fusion in the context of the functional
292 virion. Here, using cryo-ET, we have imaged the steps that an alphavirus must traverse during
293 cellular entry under near physiological conditions. This approach has enabled us to identify
294 multiple stages in the fusion process that were previously uncharacterized. By tracking the relative
295 frequency of observed states at different time points (Figure 6a), the sequence of events leading to
296 fusion and final release of the nucleocapsid was inferred (Figure 6b).

297 Whereas class-I viral fusion proteins (such as influenza HA) adopt a trimeric prefusion
298 conformation, class-II proteins in alpha- and flaviviruses are arrayed as symmetrically organized
299 heterodimers and dimers on the prefusion virion^{28,40,41}. Despite extensive quaternary interactions
300 between E1 and E2 across the icosahedrally organized virion surface, the CHIKV E1 glycoproteins
301 appear to be individually activated under the effect of low pH and membrane availability. This is
302 similar to the case in influenza virus in which individual HA activate independently and adopt
303 dynamic intermediate conformations⁴².

304 In our cryo-ET data, E1 monomers and homotrimers could be discerned in complete
305 virions, placing class-II fusion protein intermediate structures that had been characterized as
306 soluble, isolated components^{22,27,38} into the context of active membrane fusion reactions involving
307 intact particles and target membranes. Our cryo-ET analysis further corroborates the role of an
308 elongated form of E1-HT where its domain III has yet to fold back against the homotrimer core²⁷.
309 This elongated E1-HT state is somewhat analogous to the extended prehairpin intermediate
310 conformations proposed for class-I fusion proteins^{42,43}. However, there is no evidence to date that
311 extended pre-hairpin class-I trimers project into the target membrane as we observed with the
312 CHIKV E1 proteins.

313 Folding back of E1 domain III leads to colocalization of the E1 membrane anchor and its
314 FL on the same end of the protein leading to juxtaposition of viral and target membranes.
315 Supporting this notion, in our data, we first observe presence of a shortened E1-homotrimer
316 confirmation at the hemifusion stage, suggestive of E1-domain III fold-back and formation of the
317 post-fusion E1 conformation. In previous cryo-ET studies of class-I fusion proteins, the extended
318 intermediate of the glycoprotein trimer bends upon itself to bring the target membrane close to the
319 viral membrane, leading to localized dimpling of the target membrane as it is drawn towards the
320 viral membrane^{29,30}. That no such dimples were observed at any point in CHIKV class-II fusion
321 pathway indicates that there are more pathways to effect protein-mediated membrane fusion than
322 previously appreciated. In contrast, the extended, tightly docked membrane interfaces as seen in
323 CHIKV (Figure 4j,k) have been observed during influenza virus³⁰ as well as SNARE-mediated³⁹
324 membrane fusion reactions. These observations underscore the generality of this membrane
325 reorganization stage, indicating its role as an obligate intermediate state and highlighting its
326 significance in protein-mediated membrane fusion reactions.

327 Once membrane apposition occurs, the CHIKV nucleocapsid detaches from the internal
328 side of the viral membrane. This is likely necessary to provide fluidity to the viral membrane.
329 Similar disintegration of matrix layers in influenza virus membrane fusion precede fusion pore
330 formation³⁰. In our study, we also observed that under optimal fusion pH conditions, the CHIKV
331 virions, including its NC, lose their icosahedral nature. Furthermore, we observed slight expansion
332 of the glycoprotein shell in the low pH-exposed CHIKV, consistent with reports for Semliki-forest
333 virus at mildly acidic pH⁴⁴. It is possible that acid-induced conformational changes in the surface
334 glycoproteins are transmitted through the viral membrane to weaken the E2 glycoprotein's
335 cytoplasmic tail interaction with the NC⁴⁵. Loss of interaction between the external glycoproteins

336 and NC allows the glycoproteins to diffuse freely on the viral membrane, which enables direct
337 interaction between the opposing membranes during the fusion process as is seen in our study
338 (Figure 4). Changes in interaction between the E2's cytoplasmic tail and NC has been implicated
339 in causing structural changes in the NC⁴⁶. Alternatively, ion leakage across the viral membrane
340 either via the 6K protein⁴⁷ or the E1 protein⁴⁸ may permit acidification of the virus interior. It is
341 possible that both the conformational changes in the glycoproteins and acidification of the virus
342 interior mutually influence the NC structure. The present data, however, does not allow us to
343 distinguish between the two possible mechanisms. Nevertheless, it is clear that the pH-dependent
344 surface glycoprotein-NC protein interaction plays a key regulatory role in the alphavirus fusion
345 system, much like the HA-matrix protein interactions observed in influenza virus³⁰. This suggests
346 that coordinated changes between the primary fusion protein and other structural proteins in
347 enveloped viruses are a common phenomenon that likely help govern the sequence of membrane
348 fusion events.

349 One key observation regarding lipidic intermediates relates to penultimate stages of
350 membrane remodeling leading up to fusion pore opening. Notably, we observed several examples
351 of hemifused diaphragms in our data. As the time-dependent evolution of intermediate populations
352 shows (Figure 6a), a low fraction of hemifused complexes remain constant over time, even as
353 examples of post-fusion complexes increase substantially. These observations suggest that
354 hemifusion might represent a rate-limiting step in the membrane fusion process, as hypothesized
355 via fluorescence studies of CHIKV membrane fusion³³. In Ca²⁺ triggered membrane fusion
356 reactions such as the SNARE-mediated systems, the hemifused configuration has been shown to
357 embody a kinetically trapped state with productive fusion occurring instead through hemifusion-
358 free point contacts⁴⁹. In our cryo-ET data, we do not observe any examples that suggest an alternate

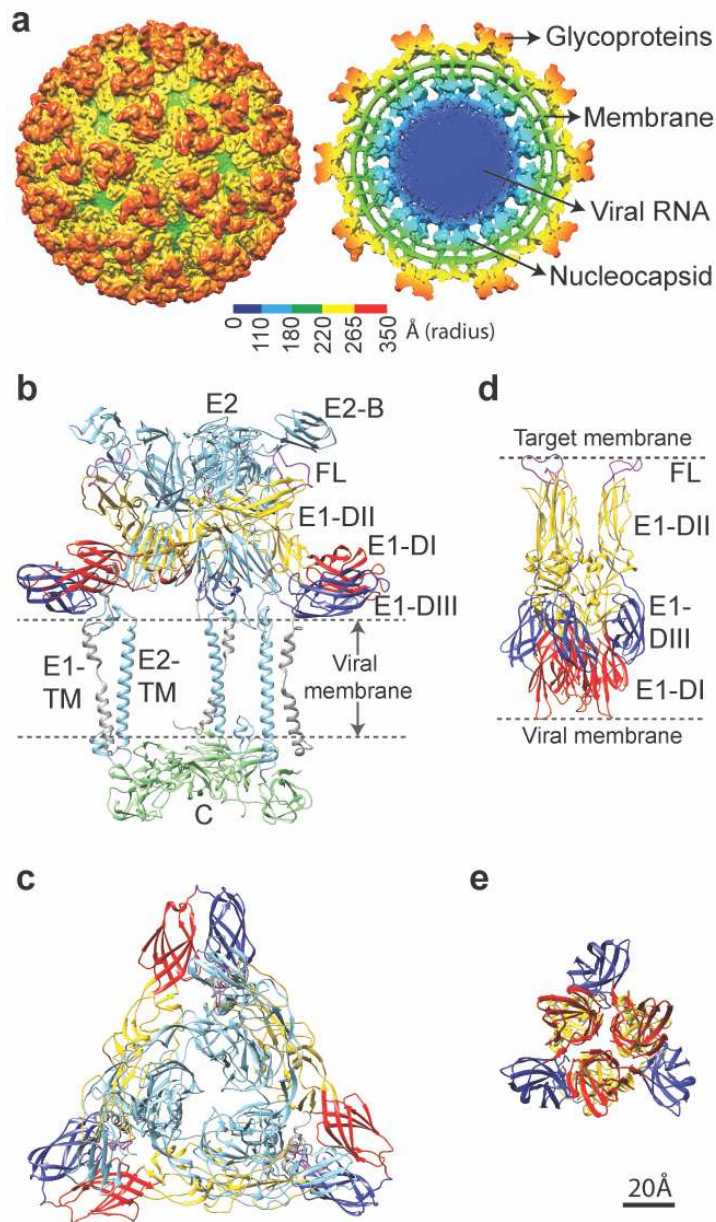
359 hemifusion-free pathway, though it is possible that such alternate pathways occur too rapidly to be
360 detected in our cryo-ET conditions.

361 The present study provides the most detailed characterization of a class-II protein-mediated
362 membrane fusion process by resolving protein intermediates and non-canonical membrane
363 configurations associated with protein remodeling. These results chart the molecular processes that
364 alphaviruses and other class-II fusion virus systems such as flaviviruses, employ in order to deliver
365 their genomes to initiate infection. With structural elucidation of these steps, it becomes possible
366 to identify key stages for targeting by inhibitors with means to understand their mechanisms. For
367 class-I fusion systems such as HIV, neutralizing antibodies have been described that bind to
368 intermediate forms of its fusion proteins and can potentially arrest the fusion process ^{50,51}. Few
369 examples of antibodies that trap flaviviruses in an intermediate stage that prevents fusion have also
370 been identified ^{52,53}. With better understanding of the key structural stages in alphavirus membrane
371 fusion, as probed in this work, it may be possible to develop better strategies to inhibit these
372 viruses' fusion and entry. At a broader level, resolving the molecular processes of CHIKV fusion
373 also advances our understanding of fundamental aspects in protein-mediated membrane fusion,
374 which is an essential biological process involved not only in enveloped virus infection but also in
375 cell-to-cell fusion, intracellular vesicle fusion, gamete fusion and synaptic vesicle signaling.

376

377

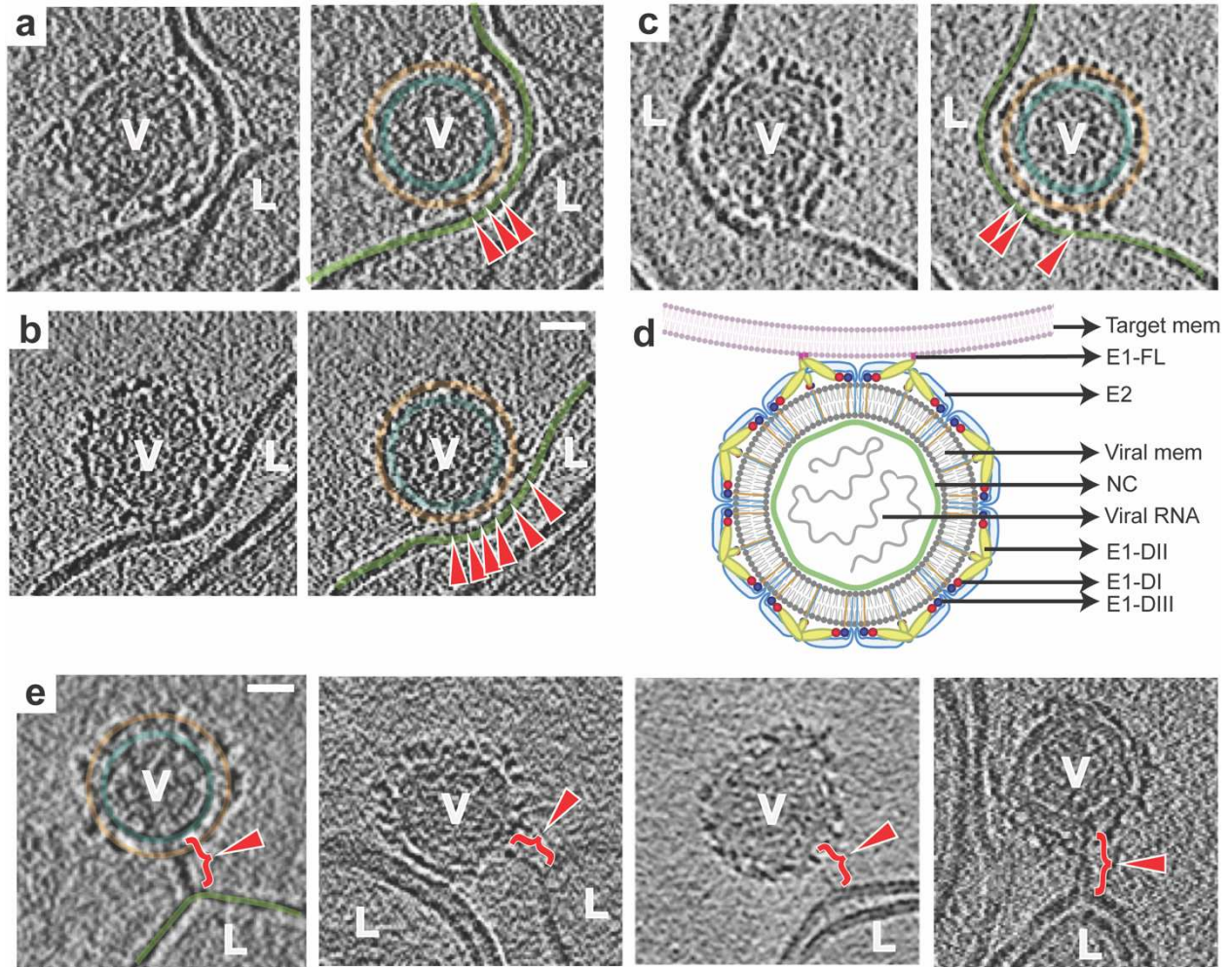
378 **Main Figures and Legends:**
379



380

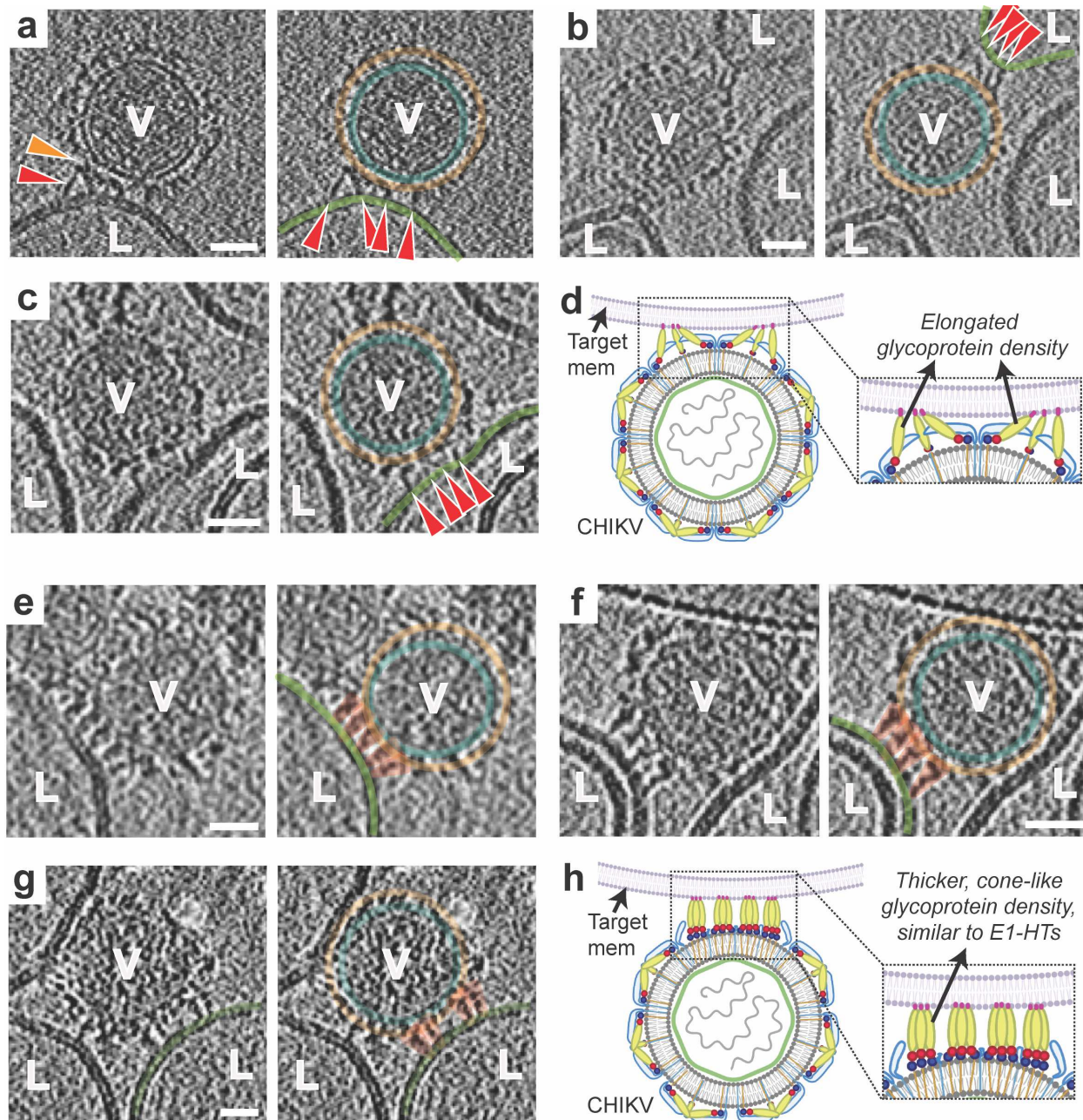
381 **Figure 1.** Structure of CHIKV particle. **a.** Surface view (left) and cross-sectional view (right) of
382 UV-inactivated CHIKV strain S27. Cryo-EM density map is colored according to radius. **b.** Side
383 view of ribbon structure of the trimeric surface glycoprotein heterodimers in contact with the inner
384 capsid protein as observed in the wild-type virion (PDB ID: 3J2W). **c.** Top view of the trimeric
385 E1-E2 heterodimers on wild-type CHIKV. **d and e.** Side and top view of the crystallographic

386 structure of post-fusion E1 homotrimers (PDB ID: 1RER) respectively. In all panels, E1 is colored
387 according to domains (domain I: red, domain II: yellow, domain III: blue, FL: magenta, E1-
388 transmembrane domain: grey), E2 is in light blue and capsid protein in green.



389

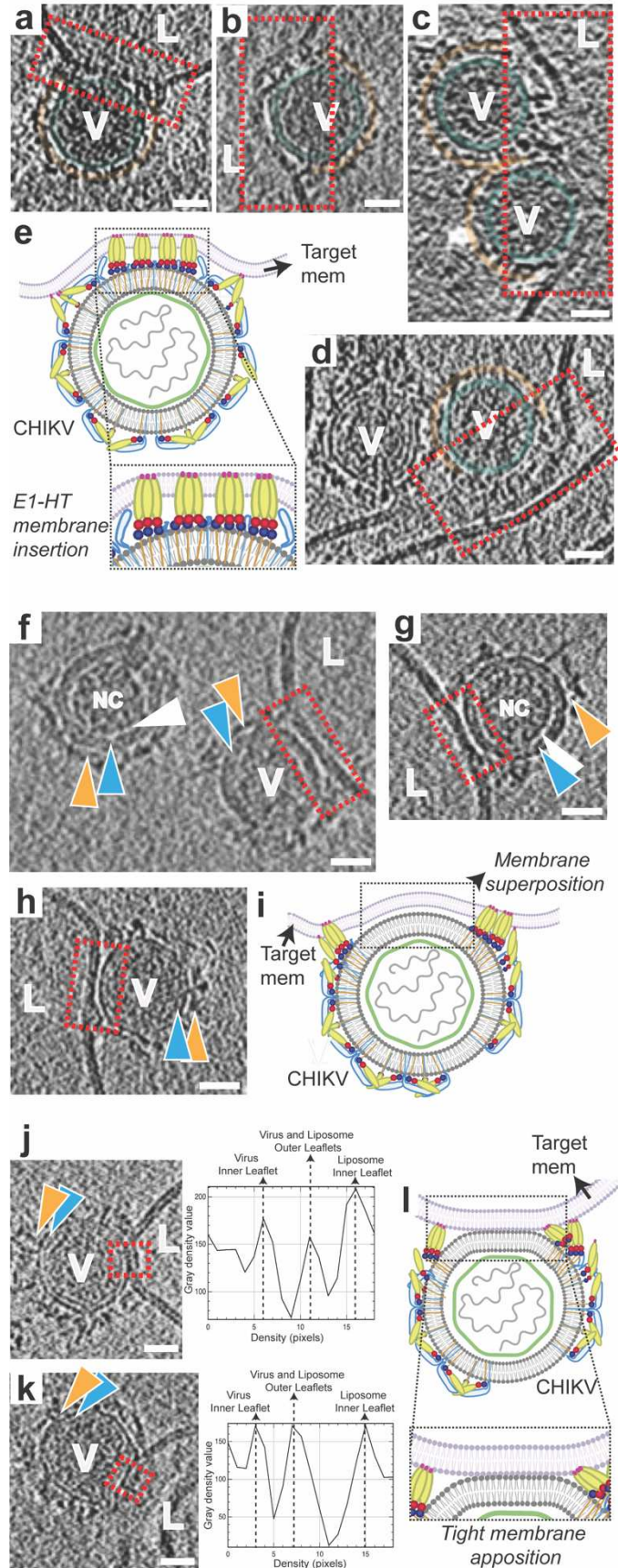
390 **Figure 2.** CHIKV membrane recruitment – stage I. **a-c.** Left panel: Tomogram slice showing
 391 CHIKV (V) interacting with liposome (L) via thin, delicate attachments. Right: Same tomogram
 392 slice as in the left panel but annotated to show the different protein and membrane layers: CHIKV
 393 glycoprotein layer in orange, CHIKV membrane in teal and liposome membrane in green. The
 394 attachments between CHIKV and liposome membrane are denoted by red arrowheads. **d.** Cartoon
 395 representation of this fusion stage. **e.** Tomogram slices showing examples of singular, long
 396 glycoprotein connection (red bracket with arrowhead) to liposome membrane. Leftmost panel
 397 alone is annotated similar to previous panels for reference. Scale bar is 200 Å in all panels. Black
 398 is high density in all panels.



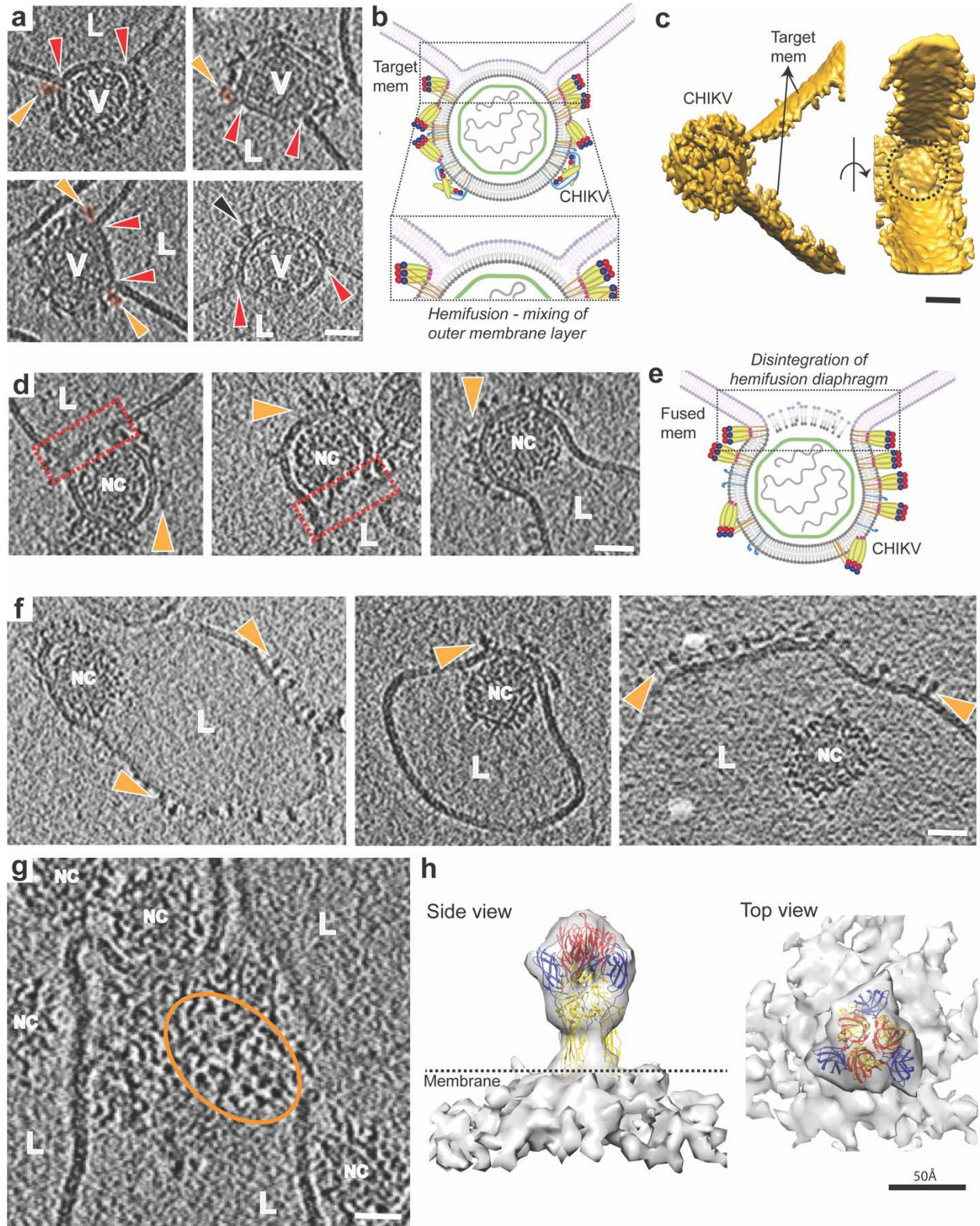
399

400 **Figure 3.** Glycoprotein membrane attachment and E1 homotrimer formation (stages II and III). a-
 401 c. Stage II. Left panels: Tomogram slice showing long bridge-like attachments between CHIKV
 402 (V) and liposomes (L). Red arrowhead indicates extended glycoprotein density and orange
 403 arrowhead denotes remaining glycoprotein density close to the viral membrane surface. Right:
 404 Same tomogram slice as in the left panels but annotated to show the different protein and
 405 membrane layers. CHIKV glycoprotein layer in orange, CHIKV membrane in teal and liposome

406 membrane in green. Glycoprotein attachments between CHIKV and liposome membrane are
407 denoted by red arrowheads. **d.** Cartoon representation of this fusion stage with zoomed inset
408 showing the virus-target membrane interaction interface. **e-g.** Stage III. Similar representation as
409 in a-c with left panels showing the raw tomogram slices and right panels showing the same slices
410 with annotation. Cone-like glycoprotein densities that resemble E1-HTs are colored in orange. **h.**
411 Cartoon representation of the E1-homotrimer formation stage with zoomed inset highlighting the
412 region of interest. Scale bar is 200 Å and black is high density in all panels.



414 **Figure 4.** E1-HT membrane insertion and opposing membrane superposition (stages IV-VI). **A-d.**
415 Annotated tomogram slices showing insertion of protein densities into the liposome (L) causing
416 disruption of membrane density at the interface. CHIKV (V) are annotated similar to previous
417 figures with red dotted rectangles enclosing interaction areas of interest. **e.** Cartoon representation
418 of fusion stage IV – E1-HT membrane insertion. **f-h.** Tomogram slices showing superposition of
419 the viral and liposome membranes. Interaction interfaces are enclosed in red rectangles. Variation
420 and fluidity in the glycoprotein layer (orange triangles) can be seen in panels f,g. White triangles
421 represent the gap observed between the NC and inner surface of the viral membrane (blue
422 triangles). **i.** Cartoon representation of fusion stage V – membrane superposition, with dotted
423 rectangle outlining the interface. **j-k.** Tomogram slices showing tightly docked membrane
424 interfaces with the proximal leaflets too close to separate at the current tomogram resolution.
425 Corresponding electron density plots along a line traversing the tight-membrane interface in the
426 boxed region (red) of the tomogram slices are also shown. **l.** Cartoon representation of the tightly
427 docked membrane interface (stage VI) with zoomed inset showing region of interest. Scale bar is
428 200 Å and black is high density in all panels.

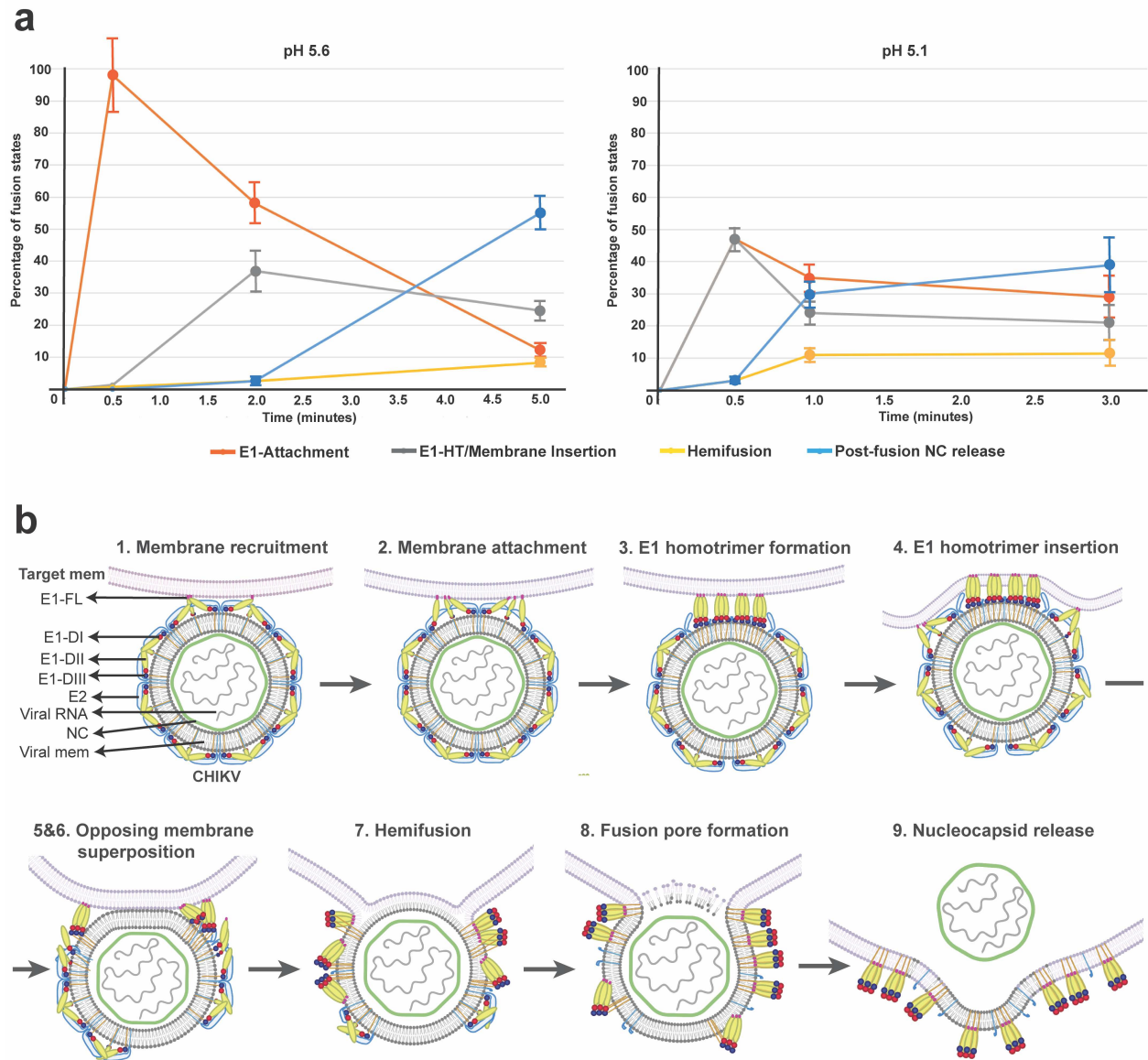


429

430 **Figure 5.** Membrane fusion stages VII -IX – hemifusion to nucleocapsid release. **a.** Tomogram

431 slices showing clear examples of hemifusion or mixing of membrane leaflets between CHIKV (V)

432 and liposomes (L). Red arrows indicate three-way junctions where the two membranes intersect.
433 Orange arrows indicate glycoprotein density (also colored in orange) at the hemifusion junction
434 that correspond to post-fusion E1 homotrimers. Black arrow shows presence of E1 homotrimers
435 on virion membrane, suggesting that E1-FL can bind to viral membrane itself on availability. **b.**
436 Cartoon representation of hemifusion with zoomed inset showing the region of mixing between
437 the two outer leaflets. **c.** Surface 3D rendering of hemifused virion shown in bottom left of panel
438 a. Side view (left) and 90° rotated view (right) is shown. The circular surface of hemifusion
439 diaphragm can be seen (black dotted circle). **d.** Disintegration of the mixed central layer in the
440 hemifused state leads to formation of a fusion pore. Fusion pore interface is shown as red
441 rectangles and glycoproteins indicated as orange triangles. **e.** Cartoon representation of panel d. **f.**
442 Subsequent release of the CHIKV nucleocapsid (NC) into the liposome lumen after fusion of the
443 viral and liposome membranes. Floating glycoprotein densities on liposome surface are indicated
444 in orange. **g.** Top view of a fused CHIKV showing triangle-shaped glycoprotein densities (orange
445 oval) on the liposome surface. **h.** Sub-tomogram average of the glycoprotein densities seen in
446 panels f and g, with the post-fusion E1-homotrimer crystal structure (PDB ID: 1RER) fitted into
447 the density. Scale bar is 200 Å and black is high density in panels a-g.



448

449 **Figure 6.** CHIKV membrane fusion pathway. **a.** Population of fusion-states during CHIKV
 450 membrane fusion. For pH 5.6 (left) and pH 5.1 (right), percentage of each fusion-state was
 451 calculated as a function of the total number of CHIKV-liposome contacts (n) observed at that given
 452 pH and timepoint. For pH 5.6, $n=281$ and for pH 5.1, $n=263$. E1 attachment (red plot line) includes
 453 stages I (membrane recruitment) and II (membrane attachment); E1-HT/Membrane Insertion (grey
 454 plot line) includes stage III-VI: E1-HT formation, E1-HT membrane insertion, membrane
 455 superposition and tight apposition; Hemifusion (yellow plot line) includes stages VII (Hemifusion)

456 and VIII (fusion pore formation); Post-fusion NC release (blue plot line) includes stage IX
457 (nucleocapsids released into liposomal lumen). Individual population counts for each state are
458 given in Supplemental Table 1. Error bars have been calculated as square root of the number of
459 complexes observed for each fusion state at the given pH and timepoint, similar to previous
460 report³⁰. **b.** Cartoon schematic of CHIKV membrane fusion stages.

461 **Methods:**

462 CHIKV preparation and purification:

463 CHIKV strain S27 was propagated and purified similar to previous reports³³. Briefly, BHK-21
464 (Baby Hamster Kidney) cells were cultured at 37C and 5% CO2 in Dubelcco's minimal essential
465 medium (DMEM) supplemented with 10% FBS (fetal bovine serum). Cells were infected with
466 virus at m.o.i of 4.0 and virus particles allowed to infect for 1.5 hours. After 25-27 hours post-
467 infection, the medium was collected, and virus particles were pelleted by ultracentrifugation for 2
468 hours at 19000rpm in a Beckman Type 19 rotor at 4°C. The pelleted virus was resuspended
469 overnight in HNE buffer (50mM HEPES, 150mM NaCl and 0.1mM EDTA), pH 7.4. The
470 resuspended sample was applied to a sucrose gradient. The sucrose gradient was spun in an
471 ultracentrifuge at 20,000rpm in a Beckman SW41 rotor overnight at 4°C. The virus band was
472 extracted, inactivated by exposure to UV lamp, aliquoted and snap frozen in liquid nitrogen. Prior
473 to experiments, inactivated CHIKV in 40% sucrose solution was dialyzed into HBS (10mM
474 HEPES, 150mM NaCl, 50mM sodium citrate) buffer pH7.5, for 4-6 hours at 4°C.

475

476 Liposome preparation:

477 Liposomes composed of phosphatidyl choline (PC), phosphatidyl ethanolamine (PE),
478 sphingomyelin and cholesterol (molar ratio 1:1:1:1.5) were prepared by lipid extrusion method
479 described previously^{30,33}. Stock solutions of the different components were prepared in chloroform
480 and combined in appropriate ratios. The combined lipid solutions were dried under nitrogen gas.
481 The lipid films were then resuspended in HBS (10mM HEPES, 150mM NaCl, 50mM sodium
482 citrate (pH 7.5) and passed through five liquid nitrogen freeze-thaw cycles. For thaw cycles, water
483 bath at 50°C was used. The resuspended solution was extruded 21 times through a 200-nm

484 polycarbonate membrane. All lipids and membrane were purchased from Avanti Polar Lipids. The
485 resulting liposomes were passed over a PD-10 desalting column (GE Healthcare) and stored in pH
486 6.0 HBS buffer.

487

488 Sample preparation and data collection for single particle cryo-EM:

489 Inactivated CHIKV in HBS buffer (pH 7.5) was applied to lacey carbon grids with a thin
490 continuous carbon film (400 mesh) (Electron Microscopy Sciences). The grids were glow
491 discharged (negative charge) under vacuum using 25mA current for 30 seconds. A 3 μ l aliquot of
492 the sample was applied to these grids at 4°C and 100% humidity, blotted for 3seconds and
493 immediately plunge frozen in liquid ethane using a Vitrobot Mark IV (FEI Co.).

494 Vitrified grids were imaged using a 300kV Titan Krios (FEI Co.) equipped with a K2
495 Summit direct electron detector (Gatan Inc.) and post-specimen energy filter. Micrographs were
496 collected at a nominal magnification of 105000X with a corresponding pixel size of 1.35 Å/pixel in
497 counting mode. A dose rate of ~ 8 e⁻/pixel/s was used with 200 ms exposure per frame and 50
498 frames per image. Data was collected with a defocus range from 1.5 to 3.5 μ m. A total of 495
499 micrographs were collected using the automated data collection software Legion⁵⁴.

500

501 Single particle cryo-EM data processing and structure determination:

502 All data processing steps were carried out within the Relion software package^{55,56}. Frame
503 alignment and dose-weighting was done using MotionCor2⁵⁷. CTF estimation was performed
504 using CTFFIND4⁵⁸. A total of 7741 particles were picked automatically using 2D reference
505 templates. Particles were extracted at 4x binning and the binned particle stack was used for
506 unsupervised 2D classification. Further processing with 3D classification did not produce any

507 individually better class. A total of 5806 selected particles were thus used for 3D refinement with
508 icosahedral symmetry imposed. Two initial models, a sphere and a low pass filtered reconstruction
509 of CHIKV virus-like particle (EMD-5580), were used for separate 3D refinement runs. Both
510 refinements converged to near identical structures of CHIKV. The particle stacks were unbinned
511 progressively for further refinements. Map sharpening and post-processing was also carried out in
512 Relion which gave a final structure with resolution 6.75 Å using the “gold-standard” FSC cutoff
513 of 0.143.

514

515 Sample preparation for cryo-ET:

516 To make grids for cryo-ET, 400 mesh Lacey carbon grids with a layer of ultrathin carbon
517 (Electron Microscopy Sciences) were glow discharged for 30 seconds. A 3µl aliquot of CHIKV
518 sample was mixed with 10nm gold beads (Aurion BSA Gold Tracer 10nm) at a ratio of 15:1 (v/v).
519 The sample was allowed to adsorb on the grid at room temperature for 15 seconds. Pre-calculated
520 volumes of liposome mixture along with appropriate volume of HBS pH 3.0 were then added to
521 the grids to drop the pH to desired values. Grids were then incubated at room temperatures for
522 different time points inside a humidity-controlled chamber to avoid evaporation. Sample grids
523 were then loaded onto a Vitrobot Mark IV (FEI Co.) at 4°C and 100% humidity, blotted for 7-
524 8seconds and plunge frozen in liquid ethane.

525

526 Cryo-ET Data collection:

527 Frozen grids were imaged using a 300 kV Titan Krios with a Gatan K2 Summit direct
528 electron detector and GIF energy filter with slit width of 20 eV. Tilt-series were collected in a
529 dose-symmetric tilting scheme from -60° to +60° or from -54° to +54° with a step size of 3° using

530 Legimon⁵⁴ or SerialEM softwares⁵⁹. Tilt-series were collected either in counting mode at a
531 magnification of 81000X, corresponding to a pixel size of 1.69 Å per pixel or in super-resolution
532 mode at a magnification of 53000X, corresponding to a pixel size of 0.8265 Å per pixel. The total
533 dose per tilt series ranged between ~60-80 e⁻/Å². A total of 441 tilt-series were collected across
534 multiple sessions.

535

536 Tomogram reconstruction:

537 Tilt-series image frames were corrected for electron beam-induced motion using
538 Motioncor2⁵⁷. Tilt images were then processed using batch tomography in IMOD⁶⁰ using standard
539 procedures to generate 3-dimensional tomogram reconstructions. Tilt-series images were aligned
540 using the gold bead markers. The aligned images were then reconstructed to give a 3D volume
541 using weighted back-projection. The final tomograms were binned, low pass-filtered and contrast
542 enhanced in ImageJ for visualization⁶¹. Supplemental tomogram movies were also made using
543 ImageJ with pixel size in direction perpendicular to electron beam (x-y direction) being 10.14
544 Å/pixel and 50.7 Å/pixel in the direction of the electron beam (z-direction). Volumes were
545 rendered in 3D using UCSF Chimera⁶².

546

547 Sub-tomogram averaging:

548 Low pH CHIKV virions and post-fusion nucleocapsids:

549 Tilt-series from pH 5.9, 5.1 and 5.1 at 30 seconds to 1 minute timepoints were imported
550 into EMAN2's sub-tomogram averaging pipeline⁶³. 1k X 1k tomograms were generated within
551 EMAN2 using default parameters. A total of 70 unattached or mildly attached virus particles were
552 picked manually in the e2spt_boxer.py interface⁶³. Sub-volumes were extracted at 8xbinning

553 corresponding to a pixel size of 6.612 Å per pixel. Sub-tomogram alignment and refinement was
554 carried using a spherical mask that covers an entire virus particle. A ring mask that encompasses
555 only the outer glycoprotein shell and membrane was also tried. Different initial models, low pass
556 filtered sphere map or CHIKV map or initial model generated within EMAN2 using stochastic
557 gradient descent principle, were used as separate starting points. In all the cases, the output map
558 did not converge to any with interpretable density features. A smaller radius mask covering only
559 the nucleocapsid region was also attempted to check if the nucleocapsid in low pH CHIKV virions
560 retained its neutral-pH structure. These attempts also failed to give any interpretable density map
561 structure. Using EMAN2 tools, 2D radial density average plot of the sub-tomogram averaged
562 CHIKV virion map was calculated for analysis.

563 A similar protocol as above was used for calculating the post-fusion nucleocapsid structure.
564 Tilt-series from later fusion timepoints were imported into the EMAN2 pipeline. Nucleocapsids
565 released into the liposome lumen were manually picked in the e2spt_boxer.py interface ⁶³. A total
566 of 122 sub-volumes that appeared reasonably spherical were extracted at 8xbinning corresponding
567 to a pixel size of 6.612 Å per pixel. A spherical mask covering the entire nucleocapsid particle was
568 used. Different initial models, low pass filtered sphere map or CHIKV nucleocapsid structure or
569 initial model generated within EMAN2 using stochastic gradient descent principle, were used as
570 separate starting points. In all cases, the output map did not converge to any interpretable density
571 features.

572

573 Post-fusion E1 glycoprotein:

574 A total of 40 tomograms from late time-points that contained fused virions with
575 distinguishable protein features on the external surface of liposomes were selected. Ctf-estimation

576 for the tilt-series was carried out in EMAN2⁶³ and ctf-correction applied using ctfplotter in
577 IMOD⁶⁴. Protein spikes on surface of liposomes were picked manually in 3d-mod⁶⁵. Each protein
578 unit was identified using two points, with first point placed distal to the membrane and the second
579 point placed at the protein end close to the membrane. Using these points, motive lists with
580 coordinate positions and rotation angles with respect to the designated 'y' axis of the tomogram
581 was calculated for each particle using the 'stalkInit' program within the PEET software suite⁶⁶. A
582 total of 591 protein spikes were picked. Subsequent sub-tomogram volume extraction, alignment
583 and averaging was also carried out within PEET using binned data corresponding to pixel size of
584 6.612 Å per pixel. A soft cylindrical mask that contained the protein spike and outer membrane
585 layer was used. Search parameters allowed for a complete 360° search along the long axis of the
586 protein spikes but restricted the search in the other two directions to ±60° with 0° being the long
587 axis of the protein spikes. Initial coarse searches were followed by progressively finer search
588 parameters. Duplicate removal was enabled to weed out overlapping volumes. Two initial models
589 were tested -- a randomly selected sub-volume and a generated map of the post-fusion E1
590 glycoprotein trimer structure from Semliki Forest virus (low pass filtered to 60Å). Missing wedge
591 compensation was also applied within PEET during the alignment and averaging process. After
592 initial alignment and averaging using standard averaging parameters as suggested by the PEET
593 tutorials, the output sub-tomogram averages from the jobs with different initial models had similar
594 structures. No symmetry was imposed in the initial steps. In the output sub-tomogram average of
595 the spike using all particles, 3-fold symmetry was observed along the long axis of the spike. The
596 dataset was spilt into even and odd datasets and averaged separately. Three-fold symmetry was
597 applied during the averaging routine to give a final density map of resolution of 27.2 Å at 0.5 FSC

598 cut-off. Crystal structure of the Semliki Forest virus post-fusion E1 glycoprotein trimer (PDB:
599 1RER) was fitted into the map density using UCSF Chimera.

600

601

602 **Acknowledgements:**

603 We thank the University of Washington Arnold and Mabel Beckman Cryo-EM for data collection
604 time and support. A portion of this research was supported by NIH grant U24GM129547 and
605 performed at the PNCC at Oregon Health and Science University (OHSU), a DOE Office of
606 Science User Facility sponsored by the Office of Biological and Environmental Research, U.S.A.

607 We also thank Dr. Mareike K. S. van Duijl-Richter, University of Groningen, Netherlands, for her
608 help in virus production. This work was supported by NIH grant R01-GM099989 (KKL).

609

610 **Author Contributions:** V.M.P.: Conceptualization, Formal analysis, Investigation, Validation
611 and Writing.; J.S.B.: Conceptualization, Resources.; J.M.S.: Resources, Writing review. K.K.L.:
612 Conceptualization, Resources, Writing, Funding acquisition.

613

614 **Competing interests:** Authors declare no competing interests.

615

616 **Data Availability:** Sub-tomogram averaged density map of post-fusion E1 trimer with
617 corresponding fitted atomic model has been deposited with accession codes EMD-XXXX and
618 PDB ID XXXX.

619

620 **References:**

- 621 1 Silva, L. A. & Dermody, T. S. Chikungunya virus: epidemiology, replication, disease
622 mechanisms, and prospective intervention strategies. *J Clin Invest* **127**, 737-749,
623 doi:10.1172/JCI84417 (2017).
- 624 2 Haider, N., Vairo, F., Ippolito, G., Zumla, A. & Kock, R. A. Basic Reproduction Number of
625 Chikungunya Virus Transmitted by Aedes Mosquitoes. *Emerg Infect Dis* **26**, 2429-2431,
626 doi:10.3201/eid2610.190957 (2020).
- 627 3 R.J., K. 629-650 (Lippincott, Williams, and Wilkins, Philadelphia, Pennsylvania, USA,
628 2013).
- 629 4 Lwande, O. W. *et al.* Global emergence of Alphaviruses that cause arthritis in humans.
630 *Infect Ecol Epidemiol* **5**, 29853, doi:10.3402/iee.v5.29853 (2015).
- 631 5 Mayer, S. V., Tesh, R. B. & Vasilakis, N. The emergence of arthropod-borne viral diseases:
632 A global prospective on dengue, chikungunya and zika fevers. *Acta Trop* **166**, 155-163,
633 doi:10.1016/j.actatropica.2016.11.020 (2017).
- 634 6 Cunha, R. V. D. & Trinta, K. S. Chikungunya virus: clinical aspects and treatment - A
635 Review. *Mem Inst Oswaldo Cruz* **112**, 523-531, doi:10.1590/0074-02760170044 (2017).
- 636 7 Dupuis-Maguiraga, L. *et al.* Chikungunya disease: infection-associated markers from the
637 acute to the chronic phase of arbovirus-induced arthralgia. *PLoS Negl Trop Dis* **6**, e1446,
638 doi:10.1371/journal.pntd.0001446 (2012).
- 639 8 Pérez-Pérez, M. J., Delang, L., Ng, L. F. P. & Priego, E. M. Chikungunya virus drug
640 discovery: still a long way to go? *Expert Opin Drug Discov* **14**, 855-866,
641 doi:10.1080/17460441.2019.1629413 (2019).
- 642 9 Gao, S., Song, S. & Zhang, L. Recent Progress in Vaccine Development Against
643 Chikungunya Virus. *Front Microbiol* **10**, 2881, doi:10.3389/fmicb.2019.02881 (2019).
- 644 10 Button, J. M., Qazi, S. A., Wang, J. C. & Mukhopadhyay, S. Revisiting an old friend: new
645 findings in alphavirus structure and assembly. *Curr Opin Virol* **45**, 25-33,
646 doi:10.1016/j.coviro.2020.06.005 (2020).

- 647 11 Sun, S. *et al.* Structural analyses at pseudo atomic resolution of Chikungunya virus and
648 antibodies show mechanisms of neutralization. *Elife* **2**, e00435, doi:10.7554/eLife.00435
649 (2013).
- 650 12 Zhang, W., Heil, M., Kuhn, R. J. & Baker, T. S. Heparin binding sites on Ross River virus
651 revealed by electron cryo-microscopy. *Virology* **332**, 511-518,
652 doi:10.1016/j.virol.2004.11.043 (2005).
- 653 13 Ubol, S. & Griffin, D. E. Identification of a putative alphavirus receptor on mouse neural
654 cells. *J Virol* **65**, 6913-6921, doi:10.1128/JVI.65.12.6913-6921.1991 (1991).
- 655 14 Tang, J. *et al.* Molecular links between the E2 envelope glycoprotein and nucleocapsid core
656 in Sindbis virus. *J Mol Biol* **414**, 442-459, doi:10.1016/j.jmb.2011.09.045 (2011).
- 657 15 Wahlberg, J. M., Bron, R., Wilschut, J. & Garoff, H. Membrane fusion of Semliki Forest
658 virus involves homotrimers of the fusion protein. *J Virol* **66**, 7309-7318,
659 doi:10.1128/JVI.66.12.7309-7318.1992 (1992).
- 660 16 Gibbons, D. L. *et al.* Multistep regulation of membrane insertion of the fusion peptide of
661 Semliki Forest virus. *J Virol* **78**, 3312-3318, doi:10.1128/jvi.78.7.3312-3318.2004 (2004).
- 662 17 Voss, J. E. *et al.* Glycoprotein organization of Chikungunya virus particles revealed by X-
663 ray crystallography. *Nature* **468**, 709-712, doi:10.1038/nature09555 (2010).
- 664 18 Hoorweg, T. E. *et al.* Dynamics of Chikungunya Virus Cell Entry Unraveled by Single-
665 Virus Tracking in Living Cells. *Journal of virology* **90**, 4745-4756, doi:10.1128/JVI.03184-
666 15 (2016).
- 667 19 Basore, K. *et al.* Cryo-EM Structure of Chikungunya Virus in Complex with the Mxra8
668 Receptor. *Cell* **177**, 1725-1737.e1716, doi:10.1016/j.cell.2019.04.006 (2019).
- 669 20 Klimstra, W. B., Nangle, E. M., Smith, M. S., Yurochko, A. D. & Ryman, K. D. DC-SIGN
670 and L-SIGN can act as attachment receptors for alphaviruses and distinguish between
671 mosquito cell- and mammalian cell-derived viruses. *J Virol* **77**, 12022-12032,
672 doi:10.1128/jvi.77.22.12022-12032.2003 (2003).
- 673 21 Wahlberg, J. M. & Garoff, H. Membrane fusion process of Semliki Forest virus. I: Low pH-
674 induced rearrangement in spike protein quaternary structure precedes virus penetration into
675 cells. *J Cell Biol* **116**, 339-348, doi:10.1083/jcb.116.2.339 (1992).

- 676 22 Gibbons, D. L. *et al.* Conformational change and protein-protein interactions of the fusion
677 protein of Semliki Forest virus. *Nature* **427**, 320-325, doi:10.1038/nature02239 (2004).
- 678 23 Klimjack, M. R., Jeffrey, S. & Kielian, M. Membrane and protein interactions of a soluble
679 form of the Semliki Forest virus fusion protein. *J Virol* **68**, 6940-6946,
680 doi:10.1128/JVI.68.11.6940-6946.1994 (1994).
- 681 24 Wengler, G. & Wörkner, D. Identification of a sequence element in the alphavirus core
682 protein which mediates interaction of cores with ribosomes and the disassembly of cores.
683 *Virology* **191**, 880-888, doi:10.1016/0042-6822(92)90263-o (1992).
- 684 25 Lanzrein, M., Schlegel, A. & Kempf, C. Entry and uncoating of enveloped viruses. *Biochem*
685 *J* **302** (Pt 2), 313-320, doi:10.1042/bj3020313 (1994).
- 686 26 Lescar, J. *et al.* The Fusion glycoprotein shell of Semliki Forest virus: an icosahedral
687 assembly primed for fusogenic activation at endosomal pH. *Cell* **105**, 137-148,
688 doi:10.1016/s0092-8674(01)00303-8 (2001).
- 689 27 Sanchez-San Martin, C., Sosa, H. & Kielian, M. A stable prefusion intermediate of the
690 alphavirus fusion protein reveals critical features of class II membrane fusion. *Cell host &*
691 *microbe* **4**, 600-608, doi:10.1016/j.chom.2008.10.012 (2008).
- 692 28 Kielian, M. & Rey, F. A. Virus membrane-fusion proteins: more than one way to make a
693 hairpin. *Nat Rev Microbiol* **4**, 67-76, doi:10.1038/nrmicro1326 (2006).
- 694 29 Lee, K. K. Architecture of a nascent viral fusion pore. *The EMBO journal* **29**, 1299-1311
695 (2010).
- 696 30 Gui, L., Ebner, J. L., Mileant, A., Williams, J. A. & Lee, K. K. Visualization and
697 Sequencing of Membrane Remodeling Leading to Influenza Virus Fusion. *J Virol* **90**, 6948-
698 6962, doi:10.1128/JVI.00240-16 (2016).
- 699 31 Calder, L. J. & Rosenthal, P. B. Cryomicroscopy provides structural snapshots of influenza
700 virus membrane fusion. *Nature structural & molecular biology* **23**, 853-858,
701 doi:10.1038/nsmb.3271 (2016).
- 702 32 Chlanda, P. *et al.* The hemifusion structure induced by influenza virus haemagglutinin is
703 determined by physical properties of the target membranes. *Nature microbiology* **1**, 16050,
704 doi:10.1038/nmicrobiol.2016.50 (2016).

- 705 33 van Duijl-Richter, M. K. S., Blijleven, J. S., van Oijen, A. M. & Smit, J. M. Chikungunya
706 virus fusion properties elucidated by single-particle and bulk approaches. *J Gen Virol* **96**,
707 2122-2132, doi:10.1099/vir.0.000144 (2015).
- 708 34 Waarts, B. L., Bittman, R. & Wilschut, J. Sphingolipid and cholesterol dependence of
709 alphavirus membrane fusion. Lack of correlation with lipid raft formation in target
710 liposomes. *J Biol Chem* **277**, 38141-38147, doi:10.1074/jbc.M206998200 (2002).
- 711 35 Smit, J. M., Bittman, R. & Wilschut, J. Low-pH-dependent fusion of Sindbis virus with
712 receptor-free cholesterol- and sphingolipid-containing liposomes. *J Virol* **73**, 8476-8484,
713 doi:10.1128/JVI.73.10.8476-8484.1999 (1999).
- 714 36 Li, L., Jose, J., Xiang, Y., Kuhn, R. J. & Rossmann, M. G. Structural changes of envelope
715 proteins during alphavirus fusion. *Nature* **468**, 705-708, doi:10.1038/nature09546 (2010).
- 716 37 Cao, S. & Zhang, W. Characterization of an early-stage fusion intermediate of Sindbis virus
717 using cryoelectron microscopy. *Proceedings of the National Academy of Sciences of the*
718 *United States of America* **110**, 13362-13367, doi:10.1073/pnas.1301911110 (2013).
- 719 38 Gibbons, D. L. *et al.* Visualization of the target-membrane-inserted fusion protein of
720 Semliki Forest virus by combined electron microscopy and crystallography. *Cell* **114**, 573-
721 583, doi:10.1016/s0092-8674(03)00683-4 (2003).
- 722 39 Witkowska, A., Heinz, L. P., Grubmuller, H. & Jahn, R. Tight docking of membranes
723 before fusion represents a metastable state with unique properties. *Nat Commun* **12**, 3606,
724 doi:10.1038/s41467-021-23722-8 (2021).
- 725 40 Harrison, S. C. Viral membrane fusion. *Virology* **479-480**, 498-507,
726 doi:10.1016/j.virol.2015.03.043 (2015).
- 727 41 Rey, F. A. & Lok, S. M. Common Features of Enveloped Viruses and Implications for
728 Immunogen Design for Next-Generation Vaccines. *Cell* **172**, 1319-1334,
729 doi:10.1016/j.cell.2018.02.054 (2018).
- 730 42 Benhaim, M. A., Mangala Prasad, V., Garcia, N. K., Guttman, M. & Lee, K. K. Structural
731 monitoring of a transient intermediate in the hemagglutinin fusion machinery on influenza
732 virions. *Sci Adv* **6**, eaaz8822, doi:10.1126/sciadv.aaz8822 (2020).

- 733 43 Benton, D. J., Gamblin, S. J., Rosenthal, P. B. & Skehel, J. J. Structural transitions in
734 influenza haemagglutinin at membrane fusion pH. *Nature* **583**, 150-153,
735 doi:10.1038/s41586-020-2333-6 (2020).
- 736 44 Haag, L. *et al.* Acid-induced movements in the glycoprotein shell of an alphavirus turn the
737 spikes into membrane fusion mode. *EMBO J* **21**, 4402-4410, doi:10.1093/emboj/cdf442
738 (2002).
- 739 45 Jose, J. *et al.* Interactions of the cytoplasmic domain of Sindbis virus E2 with nucleocapsid
740 cores promote alphavirus budding. *J Virol* **86**, 2585-2599, doi:10.1128/JVI.05860-11
741 (2012).
- 742 46 Lee, S. *et al.* Identification of a protein binding site on the surface of the alphavirus
743 nucleocapsid and its implication in virus assembly. *Structure* **4**, 531-541,
744 doi:10.1016/s0969-2126(96)00059-7 (1996).
- 745 47 Melton, J. V. *et al.* Alphavirus 6K proteins form ion channels. *J Biol Chem* **277**, 46923-
746 46931, doi:10.1074/jbc.M207847200 (2002).
- 747 48 Wengler, G., Koschinski, A. & Dreyer, F. Entry of alphaviruses at the plasma membrane
748 converts the viral surface proteins into an ion-permeable pore that can be detected by
749 electrophysiological analyses of whole-cell membrane currents. *J Gen Virol* **84**, 173-181,
750 doi:10.1099/vir.0.18696-0 (2003).
- 751 49 Diao, J. *et al.* Synaptic proteins promote calcium-triggered fast transition from point contact
752 to full fusion. *eLife* **1**, e00109, doi:10.7554/eLife.00109 (2012).
- 753 50 Caillat, C. *et al.* Structure of HIV-1 gp41 with its membrane anchors targeted by
754 neutralizing antibodies. *Elife* **10**, doi:10.7554/eLife.65005 (2021).
- 755 51 Frey, G. *et al.* A fusion-intermediate state of HIV-1 gp41 targeted by broadly neutralizing
756 antibodies. *Proceedings of the National Academy of Sciences of the United States of*
757 *America* **105**, 3739-3744, doi:10.1073/pnas.0800255105 (2008).
- 758 52 Kaufmann, B. *et al.* Capturing a flavivirus pre-fusion intermediate. *PLoS Pathog* **5**,
759 e1000672, doi:10.1371/journal.ppat.1000672 (2009).

- 760 53 Thompson, B. S. *et al.* A therapeutic antibody against west nile virus neutralizes infection
761 by blocking fusion within endosomes. *PLoS Pathog* **5**, e1000453,
762 doi:10.1371/journal.ppat.1000453 (2009).
- 763 54 Carragher, B. *et al.* Legimon: an automated system for acquisition of images from vitreous
764 ice specimens. *J Struct Biol* **132**, 33-45, doi:10.1006/jsbi.2000.4314 (2000).
- 765 55 Scheres, S. H. RELION: implementation of a Bayesian approach to cryo-EM structure
766 determination. *J Struct Biol* **180**, 519-530, doi:10.1016/j.jsb.2012.09.006 (2012).
- 767 56 Zivanov, J. *et al.* New tools for automated high-resolution cryo-EM structure determination
768 in RELION-3. *Elife* **7**, doi:10.7554/eLife.42166 (2018).
- 769 57 Zheng, S. Q. *et al.* MotionCor2: anisotropic correction of beam-induced motion for
770 improved cryo-electron microscopy. *Nat Methods* **14**, 331-332, doi:10.1038/nmeth.4193
771 (2017).
- 772 58 Rohou, A. & Grigorieff, N. CTFFIND4: Fast and accurate defocus estimation from electron
773 micrographs. *J Struct Biol* **192**, 216-221, doi:10.1016/j.jsb.2015.08.008 (2015).
- 774 59 Mastronarde, D. N. Automated electron microscope tomography using robust prediction of
775 specimen movements. *Journal of structural biology* **152**, 36-51,
776 doi:10.1016/j.jsb.2005.07.007 (2005).
- 777 60 Mastronarde, D. N. & Held, S. R. Automated tilt series alignment and tomographic
778 reconstruction in IMOD. *J Struct Biol* **197**, 102-113, doi:10.1016/j.jsb.2016.07.011 (2017).
- 779 61 Schneider, C. A., Rasband, W. S. & Eliceiri, K. W. NIH Image to ImageJ: 25 years of image
780 analysis. *Nat Methods* **9**, 671-675, doi:10.1038/nmeth.2089 (2012).
- 781 62 Pettersen, E. F. *et al.* UCSF Chimera--a visualization system for exploratory research and
782 analysis. *J Comput Chem* **25**, 1605-1612, doi:10.1002/jcc.20084 (2004).
- 783 63 Chen, M. *et al.* A complete data processing workflow for cryo-ET and subtomogram
784 averaging. *Nat Methods* **16**, 1161-1168, doi:10.1038/s41592-019-0591-8 (2019).

- 785 64 Xiong, Q., Morphew, M. K., Schwartz, C. L., Hoenger, A. H. & Mastronarde, D. N. CTF
786 determination and correction for low dose tomographic tilt series. *J Struct Biol* **168**, 378-
787 387, doi:10.1016/j.jsb.2009.08.016 (2009).
- 788 65 Kremer, J. R., Mastronarde, D. N. & McIntosh, J. R. Computer visualization of three-
789 dimensional image data using IMOD. *J Struct Biol* **116**, 71-76, doi:10.1006/jsbi.1996.0013
790 (1996).
- 791 66 Nicastro, D. *et al.* The molecular architecture of axonemes revealed by cryoelectron
792 tomography. *Science* **313**, 944-948, doi:10.1126/science.1128618 (2006).
793

Supplementary Files

This is a list of supplementary files associated with this preprint. Click to download.

- [SupplementaryInformationCHIKVKKL.docx](#)
- [SupplementalTable1.xlsx](#)
- [Supplvideo1Stage1.avi](#)
- [Supplvideo2Stage2.avi](#)
- [Supplvideo3Stage3.avi](#)
- [Supplvideo4Stage4.avi](#)
- [Supplvideo5Stage5.avi](#)
- [Supplvideo6Stage6.avi](#)
- [Supplvideo7Stage7.avi](#)
- [Supplvideo8Stage8.avi](#)
- [Supplvideo9Stage9.avi](#)